

Full paper

A cerebral cortex-like structured metallized elastomer for high-performance triboelectric nanogenerator

Moon Kyu Park^a, Seokmin Lee^a, Yongmin Ko^b, Jinhan Cho^{a,c,d,*}^a Department of Chemical & Biological Engineering, Korea University, 145 Anam-ro, Seongbuk-gu, Seoul 02841, Republic of Korea^b Division of Energy Technology, Daegu Gyeongbuk Institute of Science and Technology (DGIST), 333 Techno Jungang-daero, Hyeonpung-eup, Dalseong-gun, Daegu 42988, Republic of Korea^c KU-KIST Graduate School of Converging Science and Technology, Korea University, 145 Anam-ro, Seongbuk-gu, Seoul 02841, Republic of Korea^d Soft Hybrid Materials Research Center, Advanced Materials Research Division, Korea Institute of Science and Technology (KIST), 5 Hwarang-ro 14-gil, Seongbuk-gu, Seoul 02792, Republic of Korea

ARTICLE INFO

Keywords:

Cerebral cortex-like structure
Deformable electrode
Triboelectric nanogenerator

ABSTRACT

The advancement of wearable electronics, particularly triboelectric nanogenerators (TENGs), relies on the development of flexible, stretchable, and compressible electrodes that possess a large active surface area, high electrical conductivity, and excellent mechanical stability and deformability. However, existing elastomeric electrodes face challenges in meeting all of these requirements. Herein, we present a novel approach to address these limitations and create electrodes with elastomeric properties, stable metal-like electrical conductivity, and an expanded active surface area. For this goal, we perform an assembly of metal nanoparticles (NPs) in toluene and amine-functionalized organic linkers in alcohol onto the thiol-functionalized, embossed-structured elastomer. Particularly, the assembly process involves ligand exchange reaction-mediated metal NPs and subjecting them to solvent-swelling/deswelling of the embossed PDMS. This process induces the formation of cerebral cortex-like structured elastomer electrode, which is subsequently electroplated with Ni. The resulting electrodes exhibit metal-like electrical conductivity, elastomer-like flexibility, and cerebral cortex-like structure with substantially large surface area and high stress relieving properties. When combined with an intaglio-structured dielectric PDMS electrode, the device exhibits impressive TENG performance, surpassing the performance of conventional TENGs. This approach provides a basis for developing and designing a variety of high-performance flexible electronics, including TENGs.

1. Introduction

Flexible triboelectric nanogenerators (TENGs), which convert kinetic energy from wasted mechanical motions into electrical energy, offer a promising approach to developing a ubiquitous and transportable energy source for the next-generation portable devices, such as wearable electronics and electric skin sensors due to their simple configuration and user-friendly nature [1–9]. These devices operate by creating a potential difference through repeated contact electrification and separation of two materials with opposite triboelectric polarities, often a metal foil (e.g., aluminum, nickel, or gold) against a dielectric material such as poly(dimethylsiloxane) (PDMS), causing electric current to flow across an external circuit [10,11].

To maximize the saturating charge density of the electrode and

increase the charge generation of the TENGs, substantial research efforts have focused on increasing the surface area of dielectric materials by introducing various micro/nanostructures on the surface of elastomeric dielectric materials [12–18]. Previous works reported that increasing the deformability of the dielectric electrode with micro- and/or nanostructure could result in a significant increase in charge induction at portions of the dielectric surface not in direct contact with the metal contact electrode. This phenomenon is due to the strong electrostatic field caused by the reduction of distance between dielectric and contact electrodes during contact [19,20]. However, there have been considerable difficulties in further reducing the distance between the electrodes due to inelastic property of bulk metals as well as expanding the active surface areas of metal foil-based contact electrodes, which have limited notable enhancement of TENG performance.

* Corresponding author at: Department of Chemical & Biological Engineering, Korea University, 145 Anam-ro, Seongbuk-gu, Seoul 02841, Republic of Korea.
E-mail address: jinhan71@korea.ac.kr (J. Cho).

<https://doi.org/10.1016/j.nanoen.2023.108828>

Received 5 July 2023; Received in revised form 2 August 2023; Accepted 24 August 2023

Available online 26 August 2023

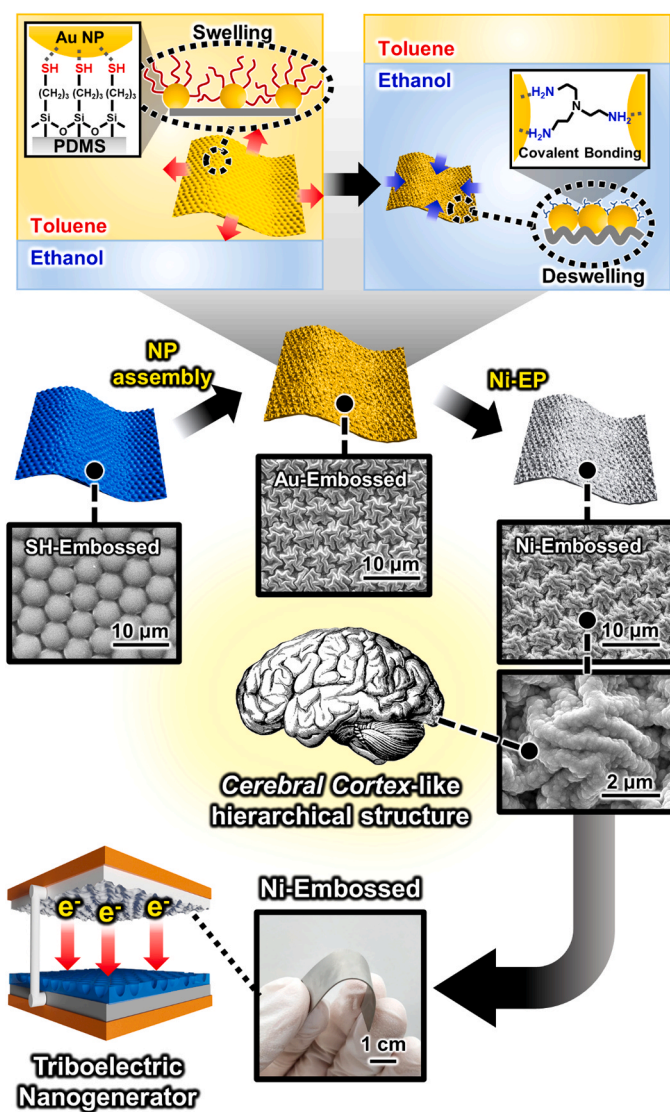
2211-2855/© 2023 The Author(s). Published by Elsevier Ltd. This is an open access article under the CC BY-NC-ND license (<http://creativecommons.org/licenses/by-nc-nd/4.0/>).

To address this limitation, significant efforts have been devoted to developing elastomer-based metallic contact electrodes with both a high surface area and deformability. Although the successful preparation of micro- or nanostructured metallic surfaces using approaches such as wet etching, laser-assisted etching, or deposition of dozens of metal nanoparticle multilayers have been reported to date [21–24], the complex fabrication processes, limited enlargement of triboelectric active area, and structural damage (by repeated contact/separation between two different triboelectric materials) have hindered the effective application of these approaches to the contact electrode of TENGs. As an alternative approach, elastic metal electrodes have primarily been achieved by depositing a thin metallic layer onto prepatterned [20,25] or mechanically pre-strained elastomer substrates [26–28]. However, the interfacial interaction between the elastomer substrate (particularly materials like PDMS) and the physically adsorbed metallic layer is poor due to the hydrophobic nature of the elastomer [27]. This unfavorable interaction negatively impacts durability of the metallic layer, leading to mechanical instability and critical failures such as delamination and cracking. Furthermore, these methods have limitations in further increasing the surface area of the electrodes and also strongly restricting the form factors of electrodes as well as the versatility of the method. Although stretchable electrodes made of conductive hydrogels and liquid metals have also been reported, these materials need to be encapsulated to maintain their mechanical properties, and therefore cannot provide a metal surface for contact with dielectric electrode [29,30].

Therefore, the development of facile solution-based approaches for creating metallized elastomer-based contact electrodes with extremely large surface area and high mechanical stability, achieved through the integration of micro- and nanostructures, along with a robust interfacial interaction between the elastomeric substrate and the metallic layer, can have tremendous potential in enabling the electrode to possess a high degree of mechanical deformability, stability, and high electrical conductivity, allowing various form factors.

Inspired by the hierarchical structure of cerebral cortex, characterized by its extraordinarily large surface area [31], our research focuses on replicating this structure on a conductive elastomer using highly favorable interfacial interactions. We anticipate that by implementing this hierarchical architecture on a conductive elastomer, it will exhibit remarkable resilience to various external stimuli, such as stretching or compression, without suffering significant damage. This property is crucial for the longevity and durability of the electrode. Moreover, when coupling the conductive elastomer with an elastomeric dielectric electrode, which also offers a substantial surface area, the resulting device comprising the dielectric and contact electrodes can effectively function as a flexible energy source. This configuration not only meets the requirements for high electric output but also ensures operational stability. Leveraging the enhanced surface area and interfacial properties, this approach can hold the potential to unlock novel possibilities in the field of various flexible electronics as well as TENGs.

In this study, we present a novel and unique elastomer electrode that mimics the intricate architecture of the cerebral cortex for TENG electrode. This electrode possesses exceptional mechanical stretchability/deformability, high electrical conductivity, and extremely large active surface area, achieved through the creation of favorable interfacial interaction- and solvent swelling/deswelling-induced adsorption of metal nanoparticles (NPs) (Scheme 1). By meticulously engineering the interface between the elastomer substrate and the metal NP layer within the metallized elastomer electrode, we establish a robust connection through covalent bonding. During the deposition of metal NPs in toluene and the subsequent introduction of molecular linker in ethanol, the embossed poly(dimethyl siloxane) (PDMS) substrate undergoes solvent swelling and deswelling processes, leading to the formation of a conductive PDMS with a structure reminiscent of the cerebral cortex. Remarkably, we demonstrate that this unique structure can be preserved even after additional metal electroplating, resulting in a perfectly metallized elastomer electrode that retains its cerebral cortex-like



Scheme 1. Schematic illustration depicting the preparation for a Ni-embossed PDMS electrode with a cerebral cortex-like structure. The fabrication process involves solvent swelling/deswelling-mediated surface wrinkling and metal electrodeposition.

structure and exceptional mechanical deformability. Furthermore, when we combine this Ni-electroplated elastomer with an elastomeric dielectric electrode featuring an intaglio structure, we witness the emergence of a highly efficient triboelectric nanogenerator (TENG) that exhibits both high electrical output and mechanical stability.

To fabricate this electrode, tetra(octyl ammonium)-stabilized Au NPs (TOABr-Au NPs) dispersed in toluene were preferentially deposited onto the thiol-functionalized PDMS (SH-PDMS) with an embossed structure. This assembly led to the formation of a densely packed array of TOABr-Au NPs on the surface of the swollen SH-PDMS film (in toluene). Subsequently, amine (NH₂)-functionalized organic linkers, tris(2-aminoethyl)amine (TREN), were assembled onto the outermost layer of the TOABr-Au NP-deposited substrate (in ethanol). In this step, the swollen TOABr-Au NP-coated PDMS with an embossed structure underwent significant shrinkage in ethanol, leading to the formation of more densely packed Au NP arrays and a surface morphology resembling the cerebral cortex. Moreover, during this transformation, the bulky hydrophobic TOABr ligands ($M_w \sim 547$) bound to the surface of Au NPs were replaced by hydrophilic TREN ligands with small molecular weight ($M_w \sim 146$). The NH₂ moieties of TREN exhibit a higher

affinity for the bare surface of Au NPs. Consequently, the embossed PDMS substrate was converted into an elastomer with a cerebral cortex-like structure and hydrophilic surface featuring periodic nanowrinkles and a sheet resistance of approximately $150 \Omega \text{ sq}^{-1}$.

Furthermore, we electroplated Ni onto the conductive and hydrophilic Au NP-assembled PDMS (i.e., outermost TREN/TOABr-Au NP/TREN/TOABr-Au NP/SH-PDMS) in an aqueous electrolyte solution. This process yielded a highly uniform, robust, and all-in-one structured Ni layer (due to the strong covalent bonding between NH_2 moieties and Ni layer) on the cerebral cortex-like structured PDMS without causing any morphological distortion. The resulting metallized elastomer exhibited a substantially low sheet resistance ($\sim 0.53 \Omega \text{ sq}^{-1}$, conductivity: $\sim 67,000 \text{ S cm}^{-1}$), excellent elastomeric properties ($\sim 23 \Omega \text{ sq}^{-1}$ at 70% strain, with only 120% of initial resistance after repetitive 20,000 cycles at 150 N compressional force), and an extremely large surface area. It should also be noted that this cerebral cortex-like structure could effectively release various external stimuli, including omnidirectional strain and compressional force. Finally, when this metallized elastomer was used as a contact electrode for the TENG, the device achieved high electrical output, generating a current and voltage output of $24.4 \mu\text{A cm}^{-2}$ and 162 V, respectively, under a compression force of 150 N. Furthermore, the TENG demonstrated exceptional operational stability, withstanding 18,000 cycles at 150 N. Considering the highly stable mechanical properties, large electrode area, and high electrical conductivity of our metallized elastomer, our approach offers a valuable tool for the development of various flexible, stretchable, and/or compressible electronic devices that require high electrical performance and diverse form factors, including TENGs.

2. Results and discussion

2.1. Preparation of cerebral cortex-like structured PDMS

To create an all-in-one metallized elastomer electrode with a cerebral cortex-like structure, we employed dry-powdered polystyrene (PS) colloids with a diameter of approximately $5 \mu\text{m}$. These colloids were mechanically rubbed against a PDMS-coated glass substrate using another PDMS film, resulting in the formation of hexagonally close-packed PS colloidal monolayers on each substrate (Fig. 1a) [32]. Subsequently, these PS colloid-assembled substrates were utilized as molds for fabricating PDMS films with a nearly perfect hexagonally packed intaglio microstructure. Moreover, the formed intaglio-PDMS film was reused as a replica mold for creating embossed micro-structured PDMS (embossed-PDMS) films with a feature size of $4.8 \mu\text{m}$ (by $5 \mu\text{m}$ PS colloids) (Fig. 1b). Notably, the hexagonally packed intaglio structures and the protuberant/embossed structures with defined diameters significantly enhanced the triboelectric surface area of the PDMS replica and the electrode, respectively, thereby influencing the amount of charge generation. Furthermore, the size of the protuberant bumps on the PDMS replica can be controlled by the diameter of the polystyrene (PS) colloids used during the mechanical rubbing process (Fig. S1).

The resulting embossed-PDMS films were further transformed into thiol-functionalized PDMS (SH-PDMS) with an embossed structure. This conversion was achieved by treating the films with (3-mercaptopropyl)trimethoxysilane, which has a strong affinity for bare metal nanoparticles such as Au NPs. This embossed SH-PDMS film (initial size $\sim 1.5 \text{ cm} \times 2.5 \text{ cm}$) was immersed in a toluene solution containing tetra(octyl ammonium bromide)-stabilized Au nanoparticles (TOABr-Au NPs) with a diameter of approximately 7 nm (Fig. S2a). As a result, the Au NPs were densely and directly deposited onto the surface of the swollen embossed SH-PDMS film (swollen size $\sim 2.1 \text{ cm} \times 3.5 \text{ cm}$) in the toluene solution. During the deposition process, the bulky TOABr ligands loosely bound to the surface of the Au NPs were replaced by the SH groups of PDMS. Subsequently, tris(2-aminoethyl)amine (TREN, $(\text{NH}_2\text{CH}_2\text{CH}_2)_3\text{N}$; molecular weight (M_w) ~ 146) in ethanol was assembled onto the TOABr-Au NP-deposited PDMS (Fig. S2b). In this case, the

NH_2 groups of TREN replaced the outermost residual TOABr ligands due to their stronger affinity for Au NPs.

To provide more conclusive evidence for the ligand exchange reactions occurring between the NH_2 groups of TREN and the TOABr ligands of Au NPs, as well as between the SH groups of PDMS and the TOABr ligands of Au NPs, the adsorption mechanism of layer-by-layer (LbL) assembled $(\text{TOABr-Au NP/TREN})_n$ multilayers was investigated on a SH-treated Si wafer using Fourier transform infrared (FTIR) spectroscopy (Figs. 1c and S3). First, when TOABr-Au NPs were deposited onto the SH-treated Si wafer substrate (i.e., $n = 0.5$), they were strongly assembled onto the substrate, resulting in the prominent C-H stretching peaks (at $2800\text{--}2950 \text{ cm}^{-1}$) originating from the bulky alkyl chains of the residual TOABr ligands bound to the top surface of Au NPs. With further deposition of NH_2 -functionalized TREN (i.e., $n = 1$), the C-H stretching peaks associated with residual TOABr ligands almost completely disappeared, indicating the complete removal of these ligands. Subsequent deposition of TOABr-Au NP/TREN multilayers resulted in a periodic change in the outermost layer from TREN to residual TOABr (bound to the surface of Au NPs) and from TOABr to TREN, as evidenced by the formation and disappearance of C-H stretching peaks. These observations provide clear evidence of the successful adsorption of $(\text{TOABr-Au NP/TREN})_n$ multilayer film onto the SH-PDMS film, facilitated by the ligand exchange reaction between the bulky TOABr ligands and TREN molecular linkers.

We also investigated the adsorption behavior of $(\text{TOABr-Au NP/TREN})_n$ multilayers using quartz crystal microbalance (QCM). The QCM data, as shown in Fig. 1d, revealed an almost linear frequency change ($-\Delta F$) of approximately 0.45 kHz per TOABr-Au NP/TREN bilayer, corresponding to an increased mass change (Δm) of $7.5 \mu\text{g cm}^{-2}$ per bilayer number (see Experimental Section). However, when the TREN layer was deposited onto the TOABr-Au NP-deposited substrate, the $-\Delta F$ (or Δm) was slightly decreased. This observation suggests that the bulky TOABr ligands ($M_w \sim 547$) were replaced by the TREN layer with an extremely low M_w (~ 146), allowing the TREN molecular layer to directly bridge the interface between adjacent Au NPs.

Although this adsorption behavior between TOABr-Au NPs and TREN in the $(\text{TOABr-Au NP/TREN})_n$ multilayers onto a robust electrode can be well addressed through QCM measurement, the adsorption behavior between the SH-PDMS substrate experiencing swelling phenomenon and TOABr-Au NPs in toluene follows a completely different adsorption mechanism. To better understand and demonstrate this unique mechanism, TOABr-Au NPs were deposited onto flat SH-PDMS instead of embossed SH-PDMS. Interestingly, with increasing adsorption time for the TOABr-Au NPs onto SH-PDMS, the adsorbed 7 nm -sized Au NPs were transformed to the Au nanomembrane layer composed of Au NPs, which induced an increase in the thickness of the Au nanomembrane (from $\sim 55 \text{ nm}$ (for 5 min) to $\sim 134 \text{ nm}$ (for 30 min)) as well as an increase in lateral size (Fig. S4). This notable phenomenon was due to the swollen PDMS surface with large amounts of thiol (SH) groups that have a higher binding affinity for the Au NP surface than the native TOABr ligands. That is, TOABr ligands loosely bound to the surfaces of Au NPs were continuously replaced by SH groups of mercaptosilane at the interface between the swollen SH-PDMS film and toluene solution, resulting in partial room-temperature melting of adjacent Au NPs without the repetitive ligand exchange processes used for TOABr-Au NPs and TREN [33]. This phenomenon can be attributed to metallic bonding between neighboring metal NPs with low cohesive energy through mutual atom diffusion, which has recently been reported to occur at small interparticle distance ($< 5.5 \text{ \AA}$) [33,34]. After the first TOABr Au NP layer ($\sim 134 \text{ nm}$ thickness for the deposition time of 30 min) is thickly deposited onto the SH-PDMS films, the increase in thickness after the deposition of second TOABr Au NP/TREN layer was measured to be about $\sim 9 \text{ nm}$, corresponding to approximately the diameter of Au NP as expected from the adsorption behavior of the typical LbL assembly (Fig. S5).

Furthermore, it is worth noting that the densely packed Au NP-

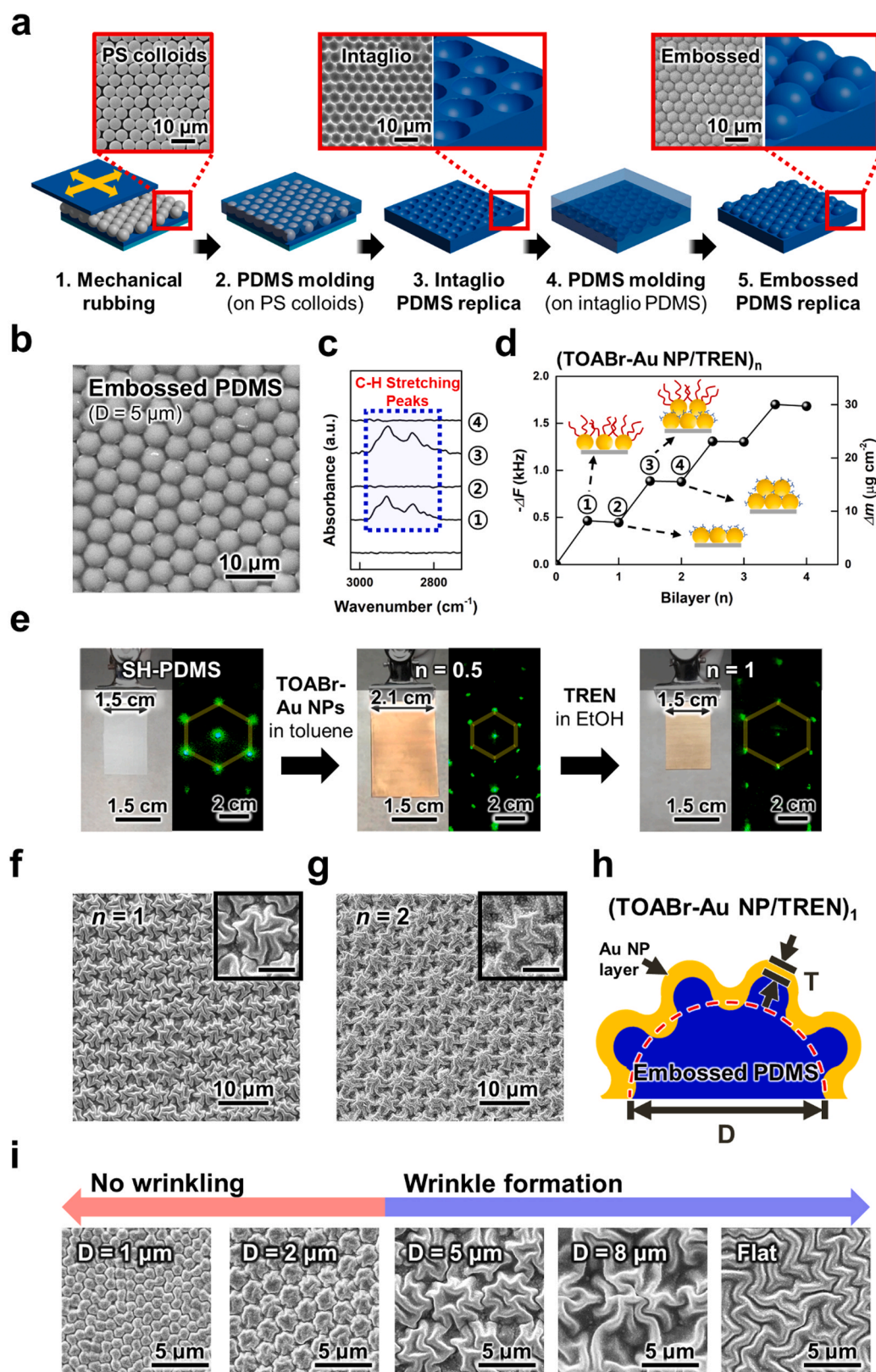


Fig. 1. (a) Schematic representation depicting the preparation of PDMS substrate with an embossed structure. (b) FE-SEM image of embossed PDMS replicated from PS colloids with diameters of 5 μm . (c) FTIR spectra of (TOABr-Au NP/TREN)_n-multilayers as a function of bilayer number (*n*). (d) QCM measurements of the decrease in frequency ($-\Delta F$, left axis) and increase in mass (Δm , right axis) with increasing bilayer numbers, and corresponding illustration of the ligand exchange mechanism at each bilayer numbers. (e) Digital images and laser diffraction pattern of embossed PDMS occurring during the deposition of (TOABr-Au NP/TREN)₁ onto SH-PDMS substrate. (f) FE-SEM images of (TOABr-Au NP/TREN)_n-embossed PDMS at $n = 1$ and (g) $n = 2$. Inset scale bars represents 5 μm in length. (h) Schematic representation of the cross-section of (TOABr-Au NP/TREN)₁-embossed PDMS. In this case, *D* and *T* represent the diameter of the embossed feature and the thickness of (TOABr-Au NP/TREN)₁ layer. (i) FE-SEM images of (TOABr-Au NP/TREN)₁-embossed PDMS with diameters ranging from $D = 1$ –8 μm and flat PDMS.

deposited PDMS with an embossed structure experienced substantial shrinkage, transitioning from the swollen film state (swollen size $\sim 2.1 \text{ cm} \times 3.5 \text{ cm}$) to its initial film state (initial size $\sim 1.5 \text{ cm} \times 2.5 \text{ cm}$) when immersed in an ethanol solution containing TREN. This shrinkage phenomenon was visually confirmed through digital photographs, laser refractive patterns, and field-emission scanning electron microscopy (FE-SEM) (Fig. 1e and f). Notably, even after undergoing shrinkage, the (TOABr-Au NP/TREN)_n-deposited embossed PDMS maintained its hexagonally embossed microstructure, despite the significant changes in pattern size. When a laser pointer was shone onto the film surface, the resultant reflection exhibited a distinct diffraction pattern, indicating the presence of periodic microstructures on the film surface (see Fig. 1e).

Another noteworthy characteristic of our approach utilizing this shrinkage effect (i.e., swelling/deswelling-mediated surface wrinkling) is the significant transformation of the pattern shape from a hexagonally packed spherical-type embossed structure (achieved by embossed SH-PDMS) to a hexagonally packed cerebral cortex-like wrinkled structure (achieved by (TOABr-Au NP/TREN)_n-PDMS) in a one step process, as depicted in field-emission scanning electron microscopy (FE-SEM) image (Fig. 1f). Energy dispersive X-ray spectroscopy (EDS) image also showed uniform deposition of Au NPs onto the SH-PDMS surface (Fig. S6). Interestingly, this unique pattern shape was established with just one bilayer deposition of TOABr-Au NP/TREN, which was evident from the negligible difference in wrinkle wavelength ($\sim 690 \pm 50 \text{ nm}$) of (TOABr-Au NP/TREN)₁- and (TOABr-Au NP/TREN)₂-PDMS films. Additionally, it should be noted that the wrinkled TOABr-Au NP layer onto SH-PDMS did not have any indication of adhesion failure such as delamination despite considerable shrinkage of PDMS substrate, which was mainly due to the strong interfacial interactions (covalent bonding) between Au NPs and SH-PDMS (Fig. S7). This seamless contact between the PDMS and the metal NP layer, coming from excellent interfacial interaction between these layers, can further enhance the mechanical stability of the elastomeric electrode.

The underlying mechanism of swelling/deswelling-mediated surface wrinkling in an embossed SH-PDMS originates from the buckling instability of the TOABr-Au NP/TREN layers that occurs to minimize the strong contractive force applied by the deswelling of the embossed SH-PDMS substrate [35]. To better understand this mechanism, the surface wrinkling in the flat PDMS was first studied before extending to that of the embossed PDMS substrate.

The wavelengths of the formed wrinkles in the flat PDMS films are governed by the following equation:

$$\lambda = 2\pi T \left(\frac{\bar{E}_f}{3E_s} \right)^{1/3} = 2\pi T \left(\frac{\bar{E}_f}{3E_s} (1 - \nu_s^2) \right)^{1/3} \quad (1)$$

where T is the thickness of the Au film, \bar{E}_f is the reduced modulus of the Au film, E_s is the Young's modulus ($\sim 2.4 \text{ MPa}$) of the PDMS substrate, and ν_s (~ 0.5) is the Poisson ratio of PDMS (Fig. S8).

As the wrinkle size and shape is almost fixed with the initial bilayer, the value of λ and T is equal to the wavelength and thickness at 1 bilayer ($\sim 1.5 \mu\text{m}$ and $\sim 134 \text{ nm}$, respectively). Based on this equation, \bar{E}_f of the deposited (TOABr-Au NP/TREN)₁ film was estimated to be approximately 54.3 MPa, which was significantly smaller than previously reported values (Young's modulus $\sim 55 \text{ GPa}$) of bulk gold thin films [36]. When the abovementioned mechanism applies for buckling instability onto the embossed PDMS substrates, the critical stress (i.e., the minimum stress required for wrinkle formation of metallic film) is significantly sensitive to surface curvature that is closely related to the feature size of the embossed structure. Previous studies on flat and curved substrates (e.g., spherical and hemispherical substrates) showed that the critical stress (σ_c^{flat} and σ_c^{curved}) has the following relationship [37–39]:

$$\sigma_c^{\text{flat}} = \frac{\bar{E}_f}{4} (3\bar{E}_s / \bar{E}_f)^{2/3} \quad (2)$$

$$\sigma_c^{\text{curved}} \approx (1 + \Omega^2) \sigma_c^{\text{flat}} \quad (3)$$

where Ω is a dimensional constant that is determined by:

$$\Omega = 4 \left(\frac{T}{D} \right) \sqrt{1 - \nu_f^2} (\bar{E}_f / 3\bar{E}_s)^{2/3} \quad (4)$$

where D is the embossed feature size (Fig. 1h).

The critical stress for wrinkling, σ_c^{curved} , is inversely proportional to the square of the feature size, D , indicating a minimum feature size at which the critical stress surpasses the deswelling stress, effectively preventing wrinkling. Feature sizes of $5 \mu\text{m}$ or larger exhibit a small difference ($< 0.5 \text{ MPa}$) between σ_c^{curved} and σ_c^{flat} , whereas feature sizes below $2 \mu\text{m}$ exhibit a rapid increase in σ_c^{curved} as the size decreases (Fig. S9). To validate these findings, we deposited a (TOABr-Au NP/TREN)₁ bilayer onto the embossed SH-PDMS substrates with feature sizes ranging from 1 to $8 \mu\text{m}$ as well as flat SH-PDMS (Fig. 1i). Our results confirmed that embossed feature sizes of $5 \mu\text{m}$ and above lead to wrinkling, while sizes of $2 \mu\text{m}$ and below did not.

Based on these results, we proceeded to investigate the electrical properties of the (TOABr-Au NP/TREN)_n-assembled PDMS films. The incorporation of the densely packed (TOABr-Au NP/TREN)₁ layer in the (TOABr-Au NP/TREN)₁-PDMS film resulted in a sheet resistance of $\sim 3 \times 10^7 \Omega \text{ sq}^{-1}$ (corresponding to electrical conductivity of approximately $2.0 \times 10^{-3} \text{ S cm}^{-1}$). However, upon depositing (TOABr-Au NP/TREN)₂, a significant decrease in sheet resistance to $150 \Omega \text{ sq}^{-1}$ (achieving an electrical conductivity of approximately 500 S cm^{-1}) was observed. This remarkable decrease in a sheet resistance in the (TOABr-Au NP/TREN)₂-PDMS film can be attributed to the reduced proximity between vertically neighboring Au NPs. Particularly, the ligand exchange from bulky TOABr to small-sized TREN linkers effectively decreased the contact resistance, thereby promoting enhanced electron transfer [40].

2.2. Ni-embossed PDMS with cerebral cortex-like structure

We expected the low sheet resistance of (TOABr-Au NP/TREN)₂-PDMS film to be sufficient for conducting Ni electroplating (at a current density of 25 mA cm^{-2}) (Fig. 2a and b). As the electroplating time progressed, the sheet resistances of the films decreased (Fig. S10), reaching $\sim 3.5 \Omega \text{ sq}^{-1}$ (with an electrical conductivity of $\sim 14,000 \text{ S cm}^{-1}$) after 30 s and $\sim 1.6 \Omega \text{ sq}^{-1}$ ($\sim 25,000 \text{ S cm}^{-1}$) after 60 s. Further electroplating up to 120 s resulted in a significant reduction of the sheet resistance to $\sim 0.53 \Omega \text{ sq}^{-1}$ ($\sim 67,000 \text{ S cm}^{-1}$), which was three orders of magnitude lower than that of the (TOABr-Au NP/TREN)₂-PDMS film (see Fig. 2b). Remarkably, the final electroplated elastomer electrode, consisting of only 2 bilayers of Au NPs, underwent a complete transition from an initially insulating elastomer substrate to a fully conductive metallized elastomer electrode. The effective coating of Ni on top of the Au NP-deposited PDMS was confirmed by X-ray diffraction (XRD) analysis and X-ray photoelectron spectroscopy (XPS) (Fig. S11).

A significant advantage of our approach is that the deposited Ni film retains the highly wrinkled structures while achieving a rapid enhancement in electrode conductivity. This outcome was made possible by the presence of hydrophilic NH_2 groups on the outermost layer of the (TOABr-Au NP/TREN)₂-PDMS film. These groups enable strong interfacial contact with the electrolyte, facilitating robust covalent bonding as Ni ions are reduced onto the electrode surface. As a result, a thin Ni layer with a thickness ranging from $\sim 65 \text{ nm}$ (achieved within 30 s electroplating time) to $\sim 140 \text{ nm}$ (achieved within 120 s electroplating time) was deposited on the (TOABr-Au NP/TREN)₂-PDMS film (Fig. S12). Planar FE-SEM images revealed that the Ni layer was deposited conformally even with increasing electroplating time (from 30 s to 120 s) (Figs. 2c and S10). The highly wrinkled microstructures,

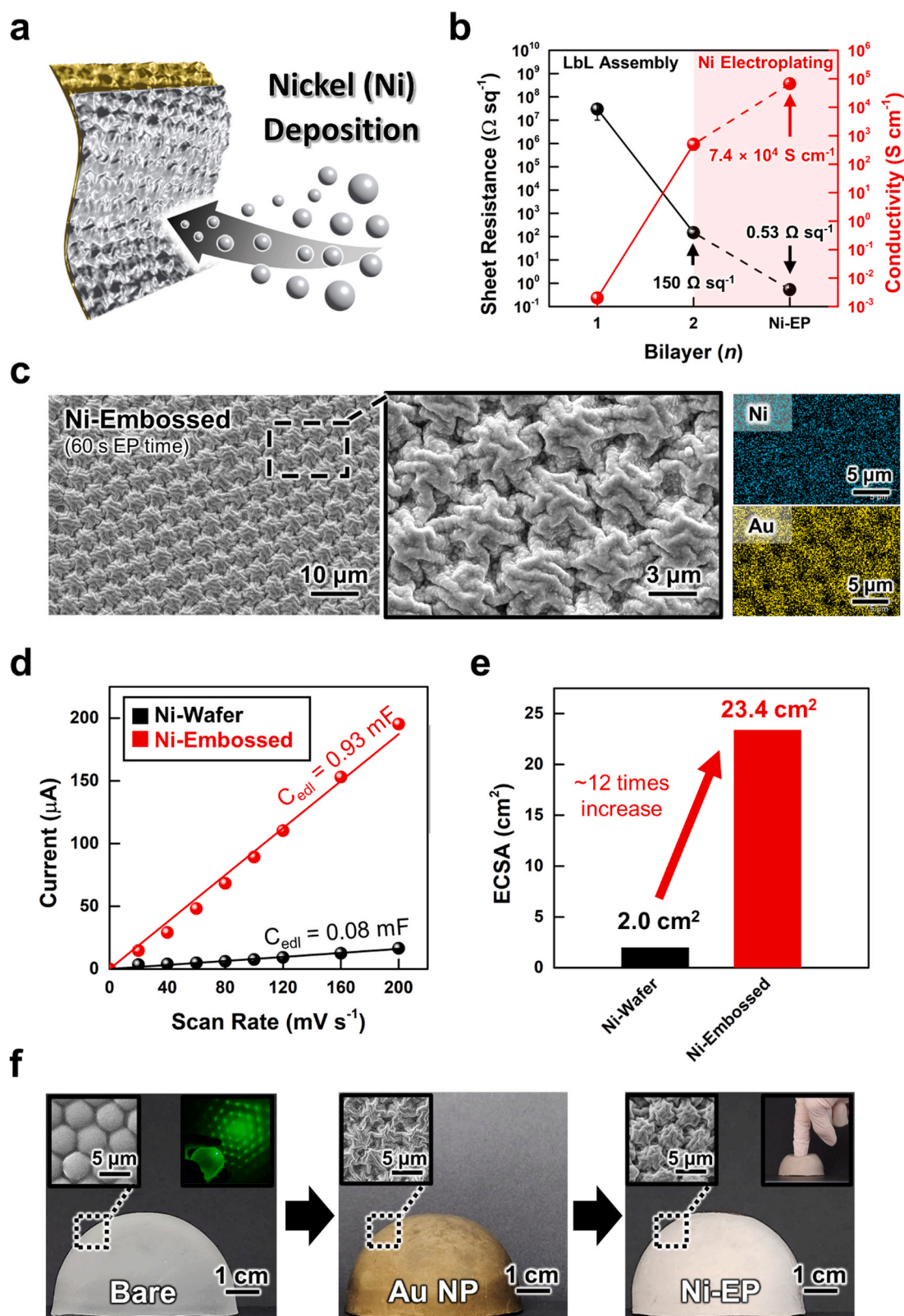


Fig. 2. (a) Schematic representation depicting Ni electrodeposition process onto cerebral cortex-like structured PDMS electrode. (b) Change in sheet resistance and conductivity of the electrode during $(\text{TOABr-Au NP/TREN})_n$ -deposition process and after Ni electroplating. (c) FE-SEM images and EDS elemental mapping images of Ni-Embossed PDMS electrode at electroplating time of 60 s (d) Current response of Ni-electroplated Si wafer (Ni-Wafer) and Ni-Embossed PDMS electrode at different scan rates (ranging from 20 to 200 mV s^{-1}). Electric double layer capacitance (C_{edl}) is obtained using the slope of the linearly fitted curve. (e) ECSA values of Ni-Wafer and Ni-Embossed PDMS electrode based on the electric double layer capacitance measurements. (f) Digital images and FE-SEM images (the left insets) of bare, Au NP-deposited, and Ni-electroplated hemispherical-shaped PDMS elastomer with embossed surface features. Transmitted laser diffraction pattern of the surface embossed patterns shown in the right inset of bare hemisphere.

with a wavelength of ~ 690 nm, remains intact, indicating conformal deposition of Ni over the pre-existing microstructures (see Fig. S10). Additionally, the FE-SEM images showed the presence of nano-sized protuberant structures, further increasing the surface area of the electrodes.

To quantify the increase in surface area of the Ni-electroplated PDMS with an embossed structure (i.e., Ni-Embossed electrode with cerebral cortex-like structure), we conducted electrochemical surface area (ECSA) measurements using cyclic voltammetry (CV) in the non-Faradic voltage range ($0\text{ V} \sim 0.1\text{ V}$) (Fig. S13) [41]. The electric double-layer capacitance (C_{edl}) was calculated from CV at different scan rates, resulting in a C_{edl} value of 0.93 mF for Ni-Embossed electrode, while Ni-electroplated wafer (i.e., Ni-Wafer) exhibited a value of 0.08 mF (Fig. 2d). These measurements indicated that the ECSA of Ni-Embossed electrode was approximately 12 times larger than that of Ni-Wafer, showing that the surface wrinkling on embossed structures significantly enhanced the surface area of the electrode compared to simple planar electrodes (Fig. 2e). This phenomenon was also supported by Brunauer–Emmett–Teller (BET) analysis of Ni-Embossed. The active surface area of Ni-Embossed electrode was measured to be $\sim 0.52\text{ m}^2\text{ g}^{-1}$, which outperformed the geometrical area ($\sim 0.004\text{ m}^2\text{ g}^{-1}$) of a flat PDMS surface with the same film thickness. (Fig. S14).

Furthermore, our approach offers a significant advantage over previous works in that it allows for facile creation of deformable elastomeric electrodes with various form factors, such as hemispherical structure, while maintaining the hierarchical surface structures described earlier. To confirm this possibility, we prepared a hemisphere-shaped PDMS with embossed surface structures (feature size of $5\text{ }\mu\text{m}$), which were subsequently assembled with (TOABr Au NP/TREN) multilayers, and further electroplated with Ni. (Fig. 2f). As a result, this approach successfully generated a hemispherical Ni elastomer with hexagonally packed cerebral cortex-like wrinkled structures, which demonstrates the ability to create a variety of metallized elastomer-based electrodes with hierarchical structure regardless of the substrate size and shape.

2.3. Mechanical properties of Ni-embossed PDMS

We performed a nanoindentation test to examine the deformability of the Ni-Embossed PDMS electrode (Fig. S15). The Ni-Embossed PDMS, electroplated for 30 s, exhibited an indentation depth of $\sim 15\text{ }\mu\text{m}$ under a maximum compressive force of 3 mN , similar to the compressibility of bare PDMS which had an indentation depth of approximately $18\text{ }\mu\text{m}$. However, a further increase of electroplating time from 30 to 120 s resulted in reduction of indentation depth due to the increase in Ni layer thickness. To maintain high conductivity and good deformability at the same time, we have fixed the electroplating time of Ni-Embossed electrodes to 60 s, which showed a sheet resistance of $\sim 1.6\text{ }\Omega\text{ sq}^{-1}$ and an indentation depth of $\sim 13\text{ }\mu\text{m}$.

Based on these results, we additionally conducted mechanical tests (i.e., bending, strain, and compression tests) that can evaluate the response of our Ni-Embossed PDMS electrodes to external mechanical stimuli. The combination of a robust percolation network resulting from the high interfacial affinity between the metallic layer and the substrate, along with the structural advantages provided by cerebral cortex-like wrinkled structure, contributed to their excellent performance. During bending tests, the resistance of the Ni-Embossed electrode increased by only around 1.7 times compared to its initial resistance, even as the radius of curvature decreased to 1.3 mm (Fig. 3a). Furthermore, the Ni-Embossed electrode maintained its electrical properties even after undergoing 10,000 bending cycles at a radius of 1.3 mm (Fig. S16). In contrast, the PDMS electrode fabricated by Au sputtering onto thiol-functionalized PDMS followed by Ni electroplating (referred to as Ni-Au sputtered electrode) showed a rapidly increasing resistance starting from a radius of 3.3 mm and became nonconductive beyond a radius of 1.9 mm .

The Ni-Embossed PDMS electrode also demonstrated high electrical stability under tensile strain, exhibiting only marginal increases in resistance ($R/R_0 \sim 15$) even when subjected to a strain of up to 70% (Fig. 3b). On the other hand, Ni-Au sputtered electrode showed a rapid rise in resistance with a slight increase in strain, resulting in significant decline in its electrical properties beyond a 15% increase in strain. This was attributed to the absence of strain-alleviating structures in Ni-Au sputtered, which resulted in the formation of visible macroscopic cracks across the electrode surface under tensile strain, ultimately compromising its mechanical performance (Fig. 3c) [42]. In stark contrast, the Ni-Embossed electrode exhibited only microscale cracking without any discernible indications of delamination of the conductive layer (Fig. 3d). Finite Element Method (FEM) simulation also revealed that stress was concentrated along the valley regions of the surface structures in the Ni-Embossed PDMS, effectively preventing the formation of macroscopic cracks by diverting crack propagation into small and narrow domains (Fig. 3e). This stress-relief mechanism contributes to the enhanced tensile stability of the Ni-Embossed electrode.

Furthermore, the Ni-Embossed electrode demonstrated excellent electrical stability under compressional force, with minimal changes in resistance even when subjected to increasing compressional forces against a bare PDMS film (ranging from 25 N to 150 N) (Fig. S17). Even after 20,000 compression cycles at a compressional force of 150 N , the electrodes showed excellent electrical stability ($R/R_0 = 1.0$) (Fig. 3f). Optical and FE-SEM observations confirmed that the surface of the electrodes exhibited no obvious signs of mechanical deterioration after compression cycling (Figs. S18 and 3g). In contrast, Ni-Au sputtered electrode showed signs of mechanical failure in the form of film detachment when compressed at 25 N . The strain-alleviating surface microstructures of the Ni-Embossed electrode, combined with the strong interfacial interaction between the PDMS substrate and the metallic film layer, contribute to its excellent stability under mechanical deformations. This makes the Ni-Embossed PDMS electrode an ideal choice for flexible, stretchable, and/or compressible electronic devices.

2.4. TENG devices based on cerebral cortex-like structured elastomer electrode

Based on the aforementioned findings, we utilized the cerebral cortex-like structured elastomer electrode (referred to as the Ni-Embossed electrode) for the fabrication of TENG devices. To assess the performance difference between TENG devices employing our elastomeric contact electrode and conventional contact electrodes, we compared their performances using a contact and separation mode-based TENG. In these TENGs, metal-based contact electrodes and dielectric electrodes come into contact and separate repeatedly, resulting in charge buildup on the dielectric electrode surface through contact electrification, which generates a potential difference during separation (Figs. S19 and S20).

For our comparative analysis, we first prepared three different types of contact electrodes: (1) Ni-Wafer without wrinkle structure as a representative of conventional rigid electrodes, (2) Ni-Flat PDMS with wrinkle structure, and (3) Ni-Embossed PDMS with a cerebral cortex-like structure. We then evaluated the triboelectric performance of these electrodes, labeled as I (Ni-Wafer) in black, II (Ni-Flat PDMS) in burgundy, and III (Ni-Embossed PDMS) in blue, against a flat PDMS film as the dielectric electrode (Fig. 4a).

When the compressive force was increased from 25 to 150 N at a frequency of 5 Hz , the output current density and open-circuit voltage of Ni-Flat/Flat PDMS-TENG was increased to $14.4\text{ }\mu\text{A cm}^{-2}$ and 110 V , respectively, surpassing the performance of Ni-Wafer/Flat PDMS-TENG (Figs. 4b-c, S21). Additionally, Ni-Embossed/Flat PDMS-TENG exhibited an output current density and voltage of $17.4\text{ }\mu\text{A cm}^{-2}$ and 128 V , respectively, which was nearly twice as high as that of Ni-Wafer/Flat PDMS-TENG. Similar trends were observed at a low compressional force of 25 N , indicating a higher electrical output of the Ni-Embossed

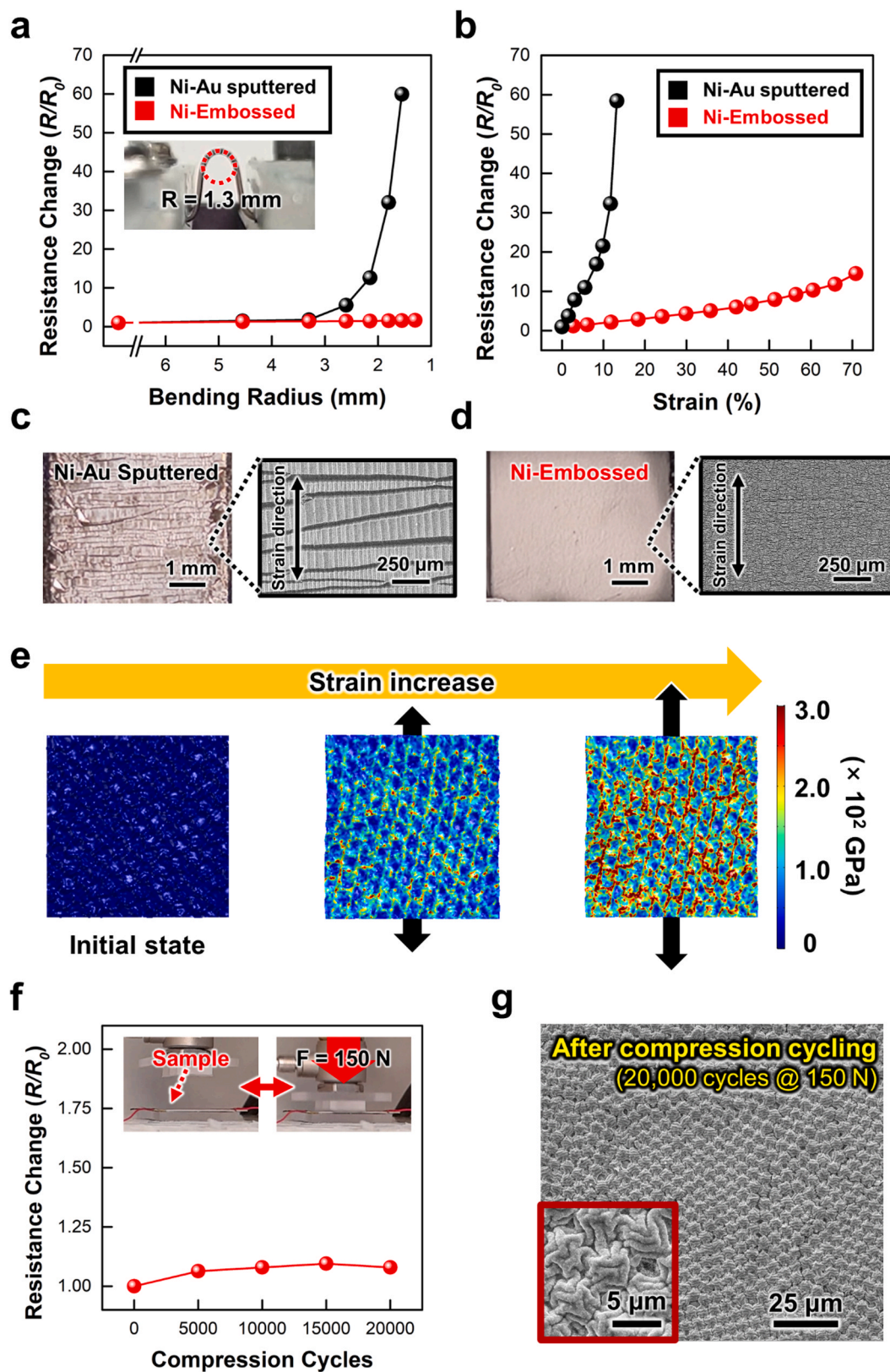


Fig. 3. (a) Resistance changes (R/R_0) of Ni-Embossed electrode and Ni-electroplated Au-sputtered PDMS (Ni-Au Sputtered) as a function of bending radius. (b) Resistance changes of Ni-Embossed and Ni-Au Sputtered electrodes as a function of tensile strain. (c) Digital images and FE-SEM images of Ni-Au Sputtered and (d) Ni-Embossed PDMS electrodes at the stretched state (strain: 50%). (e) FEM simulation showing von Mises stress distribution of the Ni layer of Ni-Embossed electrode with increasing strain. (f) Resistance changes of Ni-Embossed electrode as a function of compression cycles at a force of 150 N. (g) FE-SEM image of Ni-Embossed electrode after 20,000 compression cycles at a force of 150 N.

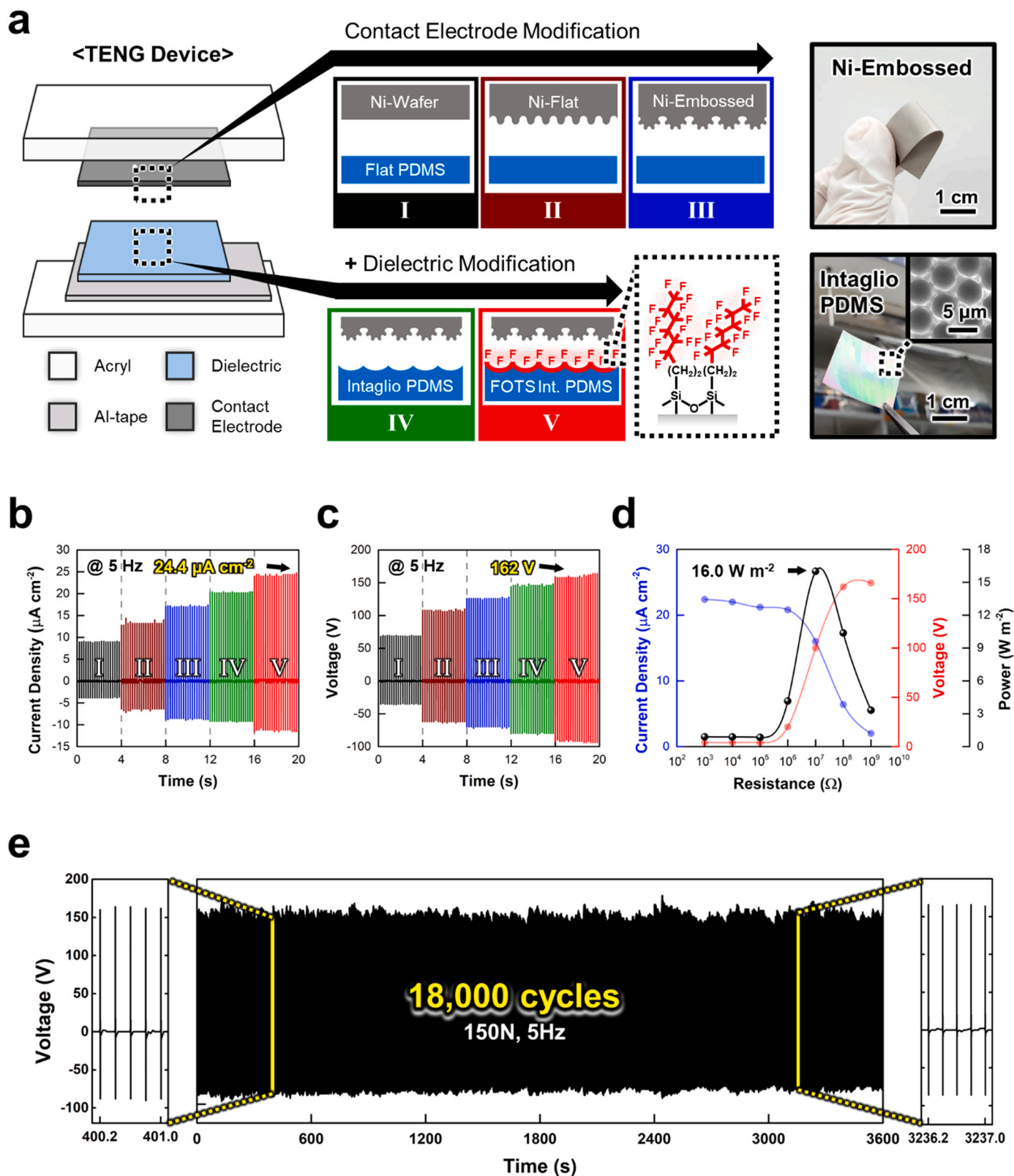


Fig. 4. (a) Schematic representation of the TENG device setup. Cross-sectional schematic representations in the middle illustrates the five different kinds (I-V) of metal contact electrode (grey) and dielectric electrode (blue) pairs used in the TENG measurements. The chemical structure shows the perfluorooctyl functional groups bonded to the dielectric electrode in the case of FOTS-Intaglio PDMS. Digital photographic images of Ni-Embossed electrode and intaglio PDMS dielectric electrode are shown in the right side. The inset of FE-SEM image displays the surface structure of the intaglio PDMS. (b) Current density and (c) open circuit voltage response of five different kinds of TENG devices. (d) Current density, open circuit voltage, and power output of Ni-Embossed/FOTS-Intaglio PDMS-TENG as a function of external resistance. (e) Stability test of Ni-Embossed/FOTS-Intaglio PDMS-TENG.

PDMS-based electrode (see Fig. S21).

The improved performance observed in the modified metal contact electrodes, particularly the Ni-Embossed electrode, can be attributed to several factors. Firstly, the presence of hierarchical micro-/nano-structured morphology on the Ni-Embossed electrode leads to an enlargement of the effective surface area compared to flat Ni-Wafer and micro-structured Ni-Flat electrodes [27]. The surface morphology, which can be controlled by increasing the initial bilayer thickness (see Fig. S4b) or changing the modulus of the PDMS substrate (i.e., by changing the thickness of the substrate), can provide a simple way to increase the surface area of the electrode. This increased surface area enhances the saturating charge density of the electrode, resulting in higher charge generation in the triboelectric nanogenerators (TENGs). This phenomenon was confirmed through analytical simulations using COMSOL software (Fig. S22). Secondly, the high deformability allows for an enlarged actual contacting area between the electrode and the dielectric, thereby increasing the triboelectric active area [43,44]. Additionally, the reduced distance between the dielectric electrode and the Ni-Embossed electrode, resulting from its high deformability, leads to an increased total capacitance difference in the TENG device [20]. This, in turn, enhances charge inducement from the electrostatic effect, contributing to the elevated electrical output of the Ni-Embossed electrode. Overall, the combination of enlarged effective surface area, increased deformability, and reduced distance in the Ni-Embossed electrode results in enhanced charge generation and improved electrical output in TENG devices.

To further enhance the triboelectric performance of the Ni-Embossed electrode, we modified the surface structure of the dielectric electrode by using a shape complementary intaglio-structured PDMS film (IV, green) and applied fluorine treatment to the intaglio PDMS (V, red) (Fig. 4a). The intaglio shape of the dielectric electrode effectively contacts the embossed structure of Ni-Embossed electrode, leading to a significant increase in the output current density and voltage of the Ni-Embossed/Intaglio PDMS-TENG [14,45]. The device exhibited a maximum output current density of $20.4 \mu\text{A cm}^{-2}$ and a voltage of 148 V (Fig. 4b and c). Furthermore, by enhancing the electronegativity of the intaglio PDMS dielectric electrode through the grafting of perfluorooctyl functional groups (i.e., FOTS-Intaglio PDMS), the charge transfer could be effectively increased from the Ni-Embossed electrode to the dielectric electrode, which could further enhance the electrical output of the Ni-Embossed/FOTS-Intaglio PDMS-TENG [46,47]. This modification resulted in a current density of $24.8 \mu\text{A cm}^{-2}$ and a voltage of 164 V. This improvement in triboelectric performance was also observed at lower compressional forces (down to 25 N), demonstrating the effective combination of Ni-Embossed electrode with surface-modified dielectric electrodes to maximize the triboelectric performance of the TENG device (Fig. S23). Additionally, we confirmed that the exact position alignment between the embossed structure of contact electrode and the intaglio structure of dielectric electrode has not significant effect on the overall triboelectric performance of TENG (Fig. S24).

We also connected resistors with values ranging from $10^3 \Omega$ to $10^9 \Omega$ to the TENG circuit as external loads to examine the instantaneous power density of the Ni-Embossed/FOTS-Intaglio PDMS-TENG (Fig. 4d). As the external resistance exceeded $10^6 \Omega$, the ohmic loss across the resistor increased rapidly, reducing the peak current density while increasing the voltage drop at the external load. Consequently, the instantaneous power density of the Ni-Embossed/FOTS-Intaglio PDMS-TENG reached a maximum value of 16.0 W m^{-2} at a resistance of $10^7 \Omega$. This indicates that the Ni-Embossed/FOTS-Intaglio PDMS-TENG can be considered a current source with a large internal resistance when the external resistance load is significantly smaller than the internal resistance. Furthermore, the Ni-Embossed/FOTS-Intaglio PDMS-TENG exhibited stable electrical output for over 18,000 compression cycles at a cycling frequency of 5 Hz and a compressional force of 150 N (Fig. 4e), highlighting the effective utilization of Ni-Embossed as a TENG electrode.

Given that both the dielectric and Ni-Embossed electrodes are composed of elastomeric materials, it is possible to create an all-elastomer-based TENG device with remarkable deformability through our approach, which is crucial for incorporation into wearable devices. Additionally, our electrodes can be made using substrates with different performance enhancing form factors (e.g., a helical structure with high stretchability or a sponge-type structure with a large surface area). This versatility enables the fabrication of TENGs for diverse applications, especially powering wearable devices.

3. Conclusion

Herein, we successfully demonstrated the fabrication of a high-performance metallized elastomer electrode with a cerebral cortex-like wrinkle structure, bulk metal-like electrical conductivity, and elastomer-like flexibility using solvent swelling/deswelling-induced metal assembly and subsequent metal electrodeposition onto SH-PDMS elastomer with an embossed structure. This approach offers several advantages over existing methods, as it eliminates the need for metal sputtering, thermal annealing, strong mechanical pressing, and/or pre-strained process to achieve high electrical conductivity and large active surface area, while also providing stable mechanical properties without the requirement for elastomeric encapsulation of conductive components. Furthermore, our approach is not limited by the substrate shape or size, allowing the fabrication of electrodes with complex morphologies required for practical use in various applications such as soft robotics, flexible energy storage systems and energy harvesting. Notably, when combined with an intaglio-structured dielectric electrode in a flexible TENG configuration, our cerebral cortex-like structured elastomer electrode exhibited remarkable performance. The resulting device achieved a current output of approximately $24.4 \mu\text{A cm}^{-2}$, a voltage output of 162 V, and excellent operational stability (during 18,000 cycles) at a compression force of 150 N, outperforming the performance of TENGs based on conventional 2D-structured metal foils. Overall, because a wide variety of active materials (such as NiCo, NiFe, etc.) can be deposited using our approach, our findings can bring significant innovation to all fields requiring stretchable electrodes with a high active surface area such as supercapacitors, Li metal batteries and water splitting. By offering a solution-processable all-in-one structured elastomer electrode with exceptional electrical and mechanical properties, we believe our findings provide a crucial foundation for future innovations in these field.

4. Experimental section

4.1. Materials

Poly(dimethylsiloxane) (Sylgard 184) was purchased from Dow Corning. Gold(III) chloride trihydrate ($\text{HAuCl}_4 \cdot 3 \text{H}_2\text{O}$), trichloro (1H,1H,2H,2H-perfluorooctyl)silane and micro particles based on polystyrene was purchased from Sigma Aldrich. Polystyrene (PS) microparticles were dried under vacuum to make into powder form. Sodium borohydride (NaBH_4) was purchased from Acros Organics. Tetraoctylammonium bromide (TOABr) and tris-(2-aminoethyl) amine (TREN) was purchased from Alfa Aesar. (3-mercaptopropyl) trimethoxysilane was purchased from Tokyo Chemical Industry. All chemical reagents were used as received without further purification.

4.2. Preparation of electrodes

4.2.1. Synthesis of toluene dispersed Au NPs

Toluene dispersed Au NPs with a diameter of 7 nm were synthesized using a modified Brust-Schiffrin method [48]. In brief, 30 mM solution of gold chloride in water was added to 25 mM solution of tetraoctylammonium bromide in toluene (80 mL) and stirred vigorously, allowing the phase transfer of the metal salt into the toluene phase. After

30 min, the water phase was removed, and 0.4 M solution of NaBH₄ in water (25 mL) was added and stirred. After 2.5 h of reduction, the toluene dispersed Au NP solution was extracted and washed for two cycles in the order of 0.1 M H₂SO₄, twice with deionized water, 0.1 M NaOH and twice with deionized water.

4.2.2. Preparation of 500 μm-thick flat/intaglio/embossed PDMS substrates

Flat PDMS film was prepared using the following method. First, the PDMS precursor and curing agent was thoroughly mixed at a 10:1 (w/w) ratio and degassed using centrifugation at 3000 rpm for 3 min. Then, the prepolymer mixture was poured onto a level, flat surface and cured at 70 °C for 3 h. The thickness of the resulting film was measured to be approximately 500 μm.

Intaglio PDMS film was prepared using the following method. First, PDMS prepolymer mixture was spin coated onto a glass slide at 1000 rpm for 30 s, and then cured at 70 °C for 3 h. After curing, polystyrene microparticles were mechanically rubbed onto the PDMS coated glass slide using another PDMS film, and then blown using an air gun to remove excess microparticles. The rubbing process led to the formation of a hexagonally packed polystyrene colloidal array [32]. Despite the absence of automated control and quantitative measurement of rubbing pressure in our study, as the process relied solely on human hands, the structural success was verified through SEM analysis.

After mechanical rubbing, the glass slide was placed on a flat, level surface, and then PDMS prepolymer mixture was poured onto the polystyrene array. The PDMS prepolymer mixture was placed in a vacuum chamber for 2 h to remove air in between the polystyrene beads, and then thermally cured at 70 °C for 3 h. The cured intaglio PDMS film was peeled from the microparticle array, and then sonicated in acetone to remove absorbed residual polystyrene.

4.2.3. Preparation of Ni-embossed PDMS electrode with cerebral cortex-like structure

Embossed PDMS substrate was first thiol functionalized using method described by Brook et al. to create a surface with high metal affinity [49]. Briefly, the embossed PDMS film was sonicated for 6 h at 50 °C in a solution of 2.65 mL (3-mercaptopropyl) trimethoxysilane and 28 mL of 1% (w/v) KOH-methanol solution. The thiolated PDMS (SH-PDMS) was then washed in fresh methanol and soaked in DCM to remove unreacted silanes.

For the preparation of nickel electroplated PDMS electrode, a conductive seed layer was first deposited onto the PDMS using a ligand exchange layer-by-layer assembly method, followed by electroplating. Conductive seed layer for nickel electroplating was prepared by alternatively depositing toluene dispersed TOABr-Au NPs (5 mg mL⁻¹) and ethanol dispersed TREN (1 mg mL⁻¹) onto the SH-PDMS substrates. The SH-PDMS substrate was dipped into TOABr-Au NP solution for 30 min, and then washed in pure toluene to detach weakly bound Au NPs. Then, the Au NP-coated sample is dipped in TREN solution for 15 min, and then washed in pure ethanol. This procedure is repeated until the sample reaches the desired conductivity for further nickel electroplating.

The prepared (TOABr-Au NP/TREN)_n multilayer coated PDMS sample was electroplated in a typical Watt bath (240 g L⁻¹ NiSO₄, 45 g L⁻¹ NiCl₂, and 30 g L⁻¹ H₃BO₃) [50]. Ni electroplating was performed using a two-electrode system, with the PDMS sample as a cathode and Ni plate as an anode. The separation distance was fixed at 2.5 cm. An external current of 25 mA cm⁻² is applied for 60 s unless specified otherwise, followed by washing in deionized water and drying in a vacuum chamber.

4.2.4. Preparation of Ni-PDMS electrode based on Au-sputtered PDMS

The experimental procedure for making Ni-PDMS electrode based on Au-sputtered PDMS (Ni-Au Sputtered PDMS) was the same as that of Ni-embossed PDMS, except that instead of TOABr-Au NP assembly, sputtering was used. Au was sputtered onto SH-PDMS using an ion sputter-

coater (MC1000, Hitachi) under a vacuum pressure of ~10⁻² Torr. Sputtering was applied at a discharge current of 15 mA. After, Ni electroplating was applied at the same condition as Ni-embossed PDMS.

4.3. Characterization

The size and shape of the TOABr-Au NPs were investigated using HR-TEM (Tecnai F20, FEI). FTIR measurements of (TOABr-Au NP/TREN)_n multilayer film on SH-treated Si wafers were made using Cary 600 spectrometer (Agilent Technologies) under advanced grazing angle (AGA) mode (resolution: 4 cm⁻¹). The FTIR peaks were plotted after baseline correction using a spectral analysis software (OMNIC, Thermo Fisher Scientific). Mass change (Δ*m*, μg cm⁻²) of (TOABr-Au NP/TREN)_n multilayer film on QCM electrode was calculated based on the frequency changes (-Δ*F*, kHz) measured using QCM 200 (SRS). This calculation was made based on the Sauerbrey Eq. (1) as follows [51]:

$$\Delta F = -2 \frac{F_0^2}{A \sqrt{\rho_q \mu_q}} \times \Delta m$$

where *F*₀, *A*, ρ_q, and μ_q represents the fundamental resonance frequency (~5 MHz), the active area (cm²), the density (2.6 mg cm⁻³), and the shear modulus (2.95 × 10¹¹ g cm⁻¹ s⁻²), respectively. By substituting the variables, this equation can be simplified into:

$$-\Delta F = 56.6 \times \Delta m$$

The surface and cross-sectional morphologies of PDMS based electrodes, along with elemental mapping were made using FE-SEM (Hitachi S4700) equipped with energy dispersive X-ray spectroscopy (EDS). The sheet resistance of the electrode was measured using a four-point probe (MCP-T610, Mitsubishi Chemical Analytech). Resistance change of the electrode during mechanical deformation was monitored using a two-point probe (Keithley 4200-SCS).

4.4. Measurement of TENG performance

TENG device was fabricated such that the separation distance between metal contact electrode and dielectric electrode was 1 cm, and the contact area of the electrodes was 1 cm × 1 cm. The thickness of the electrodes used was fixed at 500 μm. A compressive force was applied to the TENG device using a pushing tester (LabWorks, Inc., model ET-126-1), and the open-circuit voltage and short-circuit current were measured using a digital oscilloscope (Tektronix, Inc., model DMO 3052) and low-noise current preamplifier (Stanford Research Systems, Inc., model SR570). The force applied was monitored throughout the test using IEPE Mode Force Sensor (Dytran, Inc., model 10532V2).

CRedit authorship contribution statement

Moon Kyu Park: Conceptualization, Formal analysis, Investigation, Methodology, Writing – original draft. **Seokmin Lee:** Methodology, Supervision. **Yongmin Ko:** Methodology. **Jinhan Cho:** Conceptualization, Funding acquisition, Supervision, Project administration, Writing – original draft.

Declaration of Competing Interest

The authors declare that they have no known competing financial interests or personal relationships that could have appeared to influence the work reported in this paper.

Data availability

Data will be made available on request.

Acknowledgements

This work was supported by the National Research Foundation of Korea (NRF) grant funded by the Korean government (Ministry of Science and ICT) (NRF-2021R1A2C30004151) and the KU-KIST School Program.

Appendix A. Supporting information

Supplementary data associated with this article can be found in the online version at [doi:10.1016/j.nanoen.2023.108828](https://doi.org/10.1016/j.nanoen.2023.108828).

References

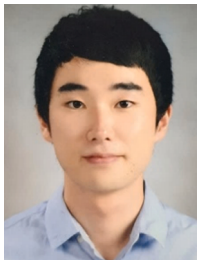
- [1] S. Wang, L. Lin, Z.L. Wang, Nanoscale triboelectric-effect-enabled energy conversion for sustainably powering portable electronics, *Nano Lett.* 12 (2012) 6339–6346.
- [2] F.R. Fan, Z.Q. Tian, Z. Lin Wang, Flexible triboelectric generator, *Nano Energy* 1 (2012) 328–334.
- [3] G. Zhu, W.Q. Yang, T. Zhang, Q. Jing, J. Chen, Y.S. Zhou, P. Bai, Z.L. Wang, Self-powered, ultrasensitive, flexible tactile sensors based on contact electrification, *Nano Lett.* 14 (2014) 3208–3213.
- [4] H. Guo, M.H. Yeh, Y.C. Lai, Y. Zi, C. Wu, Z. Wen, C. Hu, Z.L. Wang, All-in-one shape-adaptive self-charging power package for wearable electronics, *ACS Nano* 10 (2016) 10580–10588.
- [5] G. Chen, Y. Li, M. Bick, J. Chen, Smart textiles for electricity generation, *Chem. Rev.* 120 (2020) 3668–3720.
- [6] H. Kim, K.R. Pyun, M.T. Lee, H.B. Lee, S.H. Ko, Recent advances in sustainable wearable energy devices with nanoscale materials and macroscale structures, *Adv. Funct. Mater.* 32 (2022) 2110535.
- [7] H.C. Ates, P.Q. Nguyen, L. Gonzalez-Macia, E. Morales-Narváez, F. Güder, J. Collins, C. Dincer, End-to-end design of wearable sensors, *Nat. Rev. Mater.* 7 (2022) 887–907.
- [8] I. Aazem, D.T. Mathew, S. Radhakrishnan, K.V. Vijoy, H. John, D.M. Mulvihill, S. C. Pillai, Electrode materials for stretchable triboelectric nanogenerator in wearable electronics, *RSC Adv.* 12 (2022) 10545–10572.
- [9] V. Vallem, Y. Sargolzaeiavali, M. Ozturk, Y.C. Lai, M.D. Dickey, Energy harvesting and storage with soft and stretchable materials, *Adv. Mater.* 33 (2021) 2004832.
- [10] S. Niu, S. Wang, L. Lin, Y. Liu, Y.S. Zhou, Y. Hu, Z.L. Wang, Theoretical study of contact-mode triboelectric nanogenerators as an effective power source, *Energy Environ. Sci.* 6 (2013) 3576–3583.
- [11] H. Zou, Y. Zhang, L. Guo, P. Wang, X. He, G. Dai, H. Zheng, C. Chen, A.C. Wang, C. Xu, Z.L. Wang, Quantifying the triboelectric series, *Nat. Commun.* 10 (2019) 1427–1435.
- [12] F.R. Fan, L. Lin, G. Zhu, W. Wu, R. Zhang, Z.L. Wang, Transparent triboelectric nanogenerators and self-powered pressure sensors based on micropatterned plastic films, *Nano Lett.* 12 (2012) 3109–3114.
- [13] M.L. Seol, J.H. Woo, D. Il Lee, H. Im, J. Hur, Y.K. Choi, Nature-replicated nano-micro structures for triboelectric energy harvesting, *Small* 10 (2014) 3887–3894.
- [14] M. Ha, S. Lim, S. Cho, Y. Lee, S. Na, C. Baig, H. Ko, Skin-inspired hierarchical polymer architectures with gradient stiffness for spacer-free, ultrathin, and highly sensitive triboelectric sensors, *ACS Nano* 12 (2018) 3964–3974.
- [15] K.H. Ke, C.K. Chung, High-Performance Al/PDMS TENG with Novel Complex Morphology of Two-Height Microneedles Array for High-Sensitivity Force-Sensor and Self-Powered Application, *Small* 16 (2020) 2001209.
- [16] H. Niu, H. Zhang, W. Yue, S. Gao, H. Kan, C. Zhang, C. Zhang, J. Pang, Z. Lou, L. Wang, Y. Li, H. Liu, G. Shen, Micro-Nano Processing of Active Layers in Flexible Tactile Sensors via Template Methods: A Review, *Small* 17 (2021) 2100804.
- [17] Y. Jung, J. Ahn, J.S. Kim, J.H. Ha, J. Shim, H. Cho, Y.S. Oh, Y.J. Yoon, Y. Nam, I. K. Oh, J.H. Jeong, I. Park, Spherical Micro/Nano Hierarchical Structures for Energy and Water Harvesting Devices, *Small Methods* 6 (2022), 220248.
- [18] Q. Sun, Y. Lei, X. Zhao, J. Han, R. Cao, J. Zhang, W. Wu, H. Heidari, W. Li, Q. Sun, V.A.L. Roy, Scalable fabrication of hierarchically structured graphite/polydimethylsiloxane composite films for large-area triboelectric nanogenerators and self-powered tactile sensing, *Nano Energy* 80 (2021), 105521.
- [19] K.Y. Lee, J. Chun, J.H. Lee, K.N. Kim, N.R. Kang, J.Y. Kim, M.H. Kim, K.S. Shin, M. K. Gupta, J.M. Baik, S.W. Kim, Hydrophobic sponge structure-based triboelectric nanogenerator, *Adv. Mater.* 26 (2014) 5037–5042.
- [20] K.Y. Lee, H.J. Yoon, T. Jiang, X. Wen, W. Seung, S.W. Kim, Z.L. Wang, Fully Packaged Self-Powered Triboelectric Pressure Sensor Using Hemispheres-Array, *Adv. Energy Mater.* 6 (2016) 1502566.
- [21] G. Zhu, Z.H. Lin, Q. Jing, P. Bai, C. Pan, Y. Yang, Y. Zhou, Z.L. Wang, Toward large-scale energy harvesting by a nanoparticle-enhanced triboelectric nanogenerator, *Nano Lett.* 13 (2013) 847–853.
- [22] S.J. Park, M.L. Seol, D. Kim, S.B. Jeon, Y.K. Choi, Triboelectric nanogenerator with nanostructured metal surface using water-assisted oxidation, *Nano Energy* 21 (2016) 258–264.
- [23] J. Huang, X. Fu, G. Liu, S. Xu, X. Li, C. Zhang, L. Jiang, Micro/nano-structures-enhanced triboelectric nanogenerators by femtosecond laser direct writing, *Nano Energy* 62 (2019) 638–644.
- [24] S. Lee, Y. Song, Y. Ko, Y. Ko, J. Ko, C.H. Kwon, J. Huh, S.W. Kim, B. Yeom, J. Cho, A. Metal-Like, Conductive Elastomer with a Hierarchical Wrinkled Structure, *Adv. Mater.* 32 (2020) 1906460.
- [25] G. Yao, L. Xu, X. Cheng, Y. Li, X. Huang, W. Guo, S. Liu, Z.L. Wang, H. Wu, Bioinspired Triboelectric Nanogenerators as Self-Powered Electronic Skin for Robotic Tactile Sensing, *Adv. Funct. Mater.* 30 (2020) 1907312.
- [26] J. Sun, X. Pu, M. Liu, A. Yu, C. Du, J. Zhai, W. Hu, Z.L. Wang, Self-Healable, Stretchable, Transparent Triboelectric Nanogenerators as Soft Power Sources, *ACS Nano* 12 (2018) 6147–6155.
- [27] J. Ahn, Z.J. Zhao, J. Choi, Y. Jeong, S. Hwang, J. Ko, J. Gu, S. Jeon, J. Park, M. Kang, D.V. Del Orbe, I. Cho, H. Kang, M. Bok, J.H. Jeong, I. Park, Morphology-controllable wrinkled hierarchical structure and its application to superhydrophobic triboelectric nanogenerator, *Nano Energy* 85 (2021), 105978.
- [28] S. Zhang, C. Qu, Y. Xiao, H. Liu, G. Song, Y. Xu, Flexible alternating current electroluminescent devices integrated with high voltage triboelectric nanogenerators, *Nanoscale* 14 (2022) 4244–4253.
- [29] J.X. Liu, G. Liu, Z.H. Guo, W. Hu, C. Zhang, X. Pu, Electret elastomer-based stretchable triboelectric nanogenerators with autonomously managed power supplies for self-charging systems, *Chem. Eng. J.* 80 (2023), 142167.
- [30] C. Dong, A. Leber, T.D. Gupta, R. Chandran, M. Volpi, Y. Qu, T. Nguyen-Dang, N. Bartolomei, W. Yan, F. Sorin, High-efficiency super-elastic liquid metal based triboelectric fibers and textiles, *Nat. Commun.* 11 (2020) 3537.
- [31] T. Tallinen, J.Y. Chung, J.S. Biggins, L. Mahadevan, Gyration from constrained cortical expansion, *Proc. Natl. Acad. Sci. U. S. A.* 111 (2014) 12667–12672.
- [32] C. Park, T. Lee, Y. Xia, T.J. Shin, J. Myoung, U. Jeong, Quick, large-area assembly of a single-crystal monolayer of spherical particles by unidirectional rubbing, *Adv. Mater.* 26 (2014) 4633–4638.
- [33] J. Ko, C. Kim, D. Kim, Y. Song, S. Lee, B. Yeom, J. Huh, S. Han, D. Kang, J.S. Koh, J. Cho, High-performance electrified hydrogel actuators based on wrinkled nanomembrane electrodes for untethered insect-scale soft aquabots, *Sci. Robot.* 7 (2022) eabo6463.
- [34] J.N. Israelachvili, Van der Waals forces between particles and surfaces, in: J. N. Israelachvili (Ed.), *Intermolecular and Surface Forces*, 3rd ed., Academic Press, 2011, pp. 253–289.
- [35] J.Y. Chung, A.J. Nolte, C.M. Stafford, Surface wrinkling: A versatile platform for measuring thin-film properties, *Adv. Mater.* 23 (2011) 349–368.
- [36] H.D. Espinosa, B.C. Prorok, Size effects on the mechanical behavior of gold thin films, *J. Mater. Sci.* 38 (2003) 4125–4128.
- [37] G. Cao, X. Chen, C. Li, A. Ji, Z. Cao, Self-assembled triangular and labyrinth buckling patterns of thin films on spherical substrates, *Phys. Rev. Lett.* 100 (2008), 036102.
- [38] D. Breid, A.J. Crosby, Curvature-controlled wrinkle morphologies, *Soft Matter* 9 (2013) 3624–3630.
- [39] J. Yin, X. Han, Y. Cao, C. Lu, Surface wrinkling on polydimethylsiloxane microspheres via wet surface chemical oxidation, *Sci. Rep.* 4 (2014) 5710.
- [40] Y. Ko, C.H. Kwon, S.W. Lee, J. Cho, Nanoparticle-based electrodes with high charge transfer efficiency through ligand exchange layer-by-layer assembly, *Adv. Mater.* 32 (2020) 2001924.
- [41] E. Cossar, M.S.E. Houache, Z. Zhang, E.A. Baranova, Comparison of electrochemical active surface area methods for various nickel nanostructures, *J. Electroanal. Chem.* 870 (2020), 114246.
- [42] C. Cho, P. Kang, A. Taqieuddin, Y. Jing, K. Yong, J.M. Kim, M.F. Haque, N.R. Aluru, S.W. Nam, Strain-resilient electrical functionality in thin-film metal electrodes using two-dimensional interlayers, *Nat. Electron.* 4 (2021) 126–133.
- [43] J.H. Lee, I. Yu, S. Hyun, J.K. Kim, U. Jeong, Remarkable increase in triboelectrification by enhancing the conformable contact and adhesion energy with a film-covered pillar structure, *Nano Energy* 34 (2017) 233–241.
- [44] Y. Liu, W. Liu, Z. Wang, W. He, Q. Tang, Y. Xi, X. Wang, H. Guo, C. Hu, Quantifying contact status and the air-breakdown model of charge-excitation triboelectric nanogenerators to maximize charge density, *Nat. Commun.* 11 (2020) 1–8.
- [45] X.W. Zhang, G.Z. Li, G.G. Wang, J.L. Tian, Y.L. Liu, D.M. Ye, Z. Liu, H.Y. Zhang, J. C. Han, High-Performance Triboelectric Nanogenerator with Double-Surface Shape-Complementary Microstructures Prepared by Using Simple Sandpaper Templates, *ACS Sustain. Chem. Eng.* 6 (2018) 2283–2291.
- [46] G. Song, Y. Kim, S. Yu, M.O. Kim, S.H. Park, S.M. Cho, D.B. Velusamy, S.H. Cho, K. L. Kim, J. Kim, E. Kim, C. Park, Molecularly Engineered Surface Triboelectric Nanogenerator by Self-Assembled Monolayers (METS), *Chem. Mater.* 27 (2015) 4749–4755.
- [47] Y. Liu, J. Mo, Q. Fu, Y. Lu, N. Zhang, S. Wang, S. Nie, Enhancement of triboelectric charge density by chemical functionalization, *Adv. Funct. Mater.* 30 (2020) 2004714.
- [48] J. Fink, C.J. Kiely, D. Bethell, D.J. Schiffrin, Self-organization of nanosized gold particles, *Chem. Mater.* 10 (1998) 922–926.
- [49] J. Zhang, Y. Chen, M.A. Brook, Facile functionalization of PDMS elastomer surfaces using thiol-ene click chemistry, *Langmuir* 29 (2013) 12432–12442.
- [50] O.P. Watts, Rapid nickel plating, *Trans. Am. Electrochem. Soc.* 29 (1916) 395–403.
- [51] D.A. Buttry, *Applications of the QCM to Electrochemistry*, Marcel Dekker Inc., New York, 1991.



Moon Kyu Park is a MS candidate under Prof. Jinhan Cho at the Department of Chemical and Biological Engineering in Korea University. Currently, his research interest is focused on the development of novel elastomeric electrodes and their applications.



Yongmin Ko received his Ph. D degree at the Department of Chemical and Biological Engineering in Korea University in 2016. He was a postdoctoral researcher at Georgia Institute of Technology in Atlanta until 2019. Currently, he is working as a senior researcher at the Division of Energy Technology at the Daegu Gyeongbuk Institute of Science and Technology (DGIST) in Republic of Korea. His research interest is focused on energy conversion and storage devices based on various functional nanomaterials.



Seokmin Lee is a Ph.D. candidate under Prof. Jinhan Cho at the Department of Chemical and Biological Engineering in Korea University. Currently, his research interest is focused on flexible/stretchable energy electrodes based on the interfacial engineering of functional nanomaterials.



Jinhan Cho is a professor at the Department of Chemical & Biological Engineering in Korea University since 2010. His research career started in POSTECH and Seoul National University, where he completed his M.S. and Ph.D. degrees in 1997 and 2001, respectively. Then, he worked as a postdoctoral researcher at Max Planck Institute of Colloids and Interface and University of Melbourne. In 2003–2005, he was a senior researcher in LG Chemistry R&D center. In 2006–2010, he worked as an assistant professor in Kookmin University. His research interests have been focused on studying the surface chemistry and electrochemical properties of various electrode materials.